

Silicon nanoparticle generation and deposition on glass from waste silicon powder by nanosecond pulsed laser irradiation

Ko Momoki ^a, Takeshi Manabe ^b, Lin Li ^c, Jiwang Yan ^{a,d,*}

^a School of Integrated Design Engineering, Graduate School of Science and Technology, Keio University, Hiyoshi 3-14-1, Kohoku-ku, Yokohama, 223-8522, Japan

^b Rayconnect, Inc., 1955-1, Kurematsu-cho, Nishi-ku, Hamamatsu, Shizuoka, 431-1202, Japan

^c Laser Processing Research Centre, Department of Mechanical, Aerospace and Civil Engineering, Faculty of Science and Engineering, The University of Manchester, Manchester, M13 9PL, UK

^d Department of Mechanical Engineering, Faculty of Science and Technology, Keio University, Hiyoshi 3-14-1, Kohoku-ku, Yokohama, 223-8522, Japan

ARTICLE INFO

Keywords:

Silicon crystal
Nanoparticle
Nanosecond pulsed laser
Raman spectroscopy
Waste silicon powder

ABSTRACT

Silicon nanoparticles can be used for fabricating electrodes in high-performance lithium ion batteries and other high value-added products. Currently, silicon nanoparticles are fabricated by pulsed laser irradiation of single-crystal silicon wafers in water. In this study, we proposed silicon nanoparticle generation by using a nanosecond pulsed laser to irradiate waste silicon powder which is disposed from wire-saw slicing processes of silicon ingots. The laser-induced nanoparticles were backward-transferred and deposited on a glass substrate. It was found that the morphology and amount of the deposited nanoparticles was strongly dependent on the distance between the glass substrate and the waste silicon powder target. Raman spectroscopy showed that the silicon nanoparticles were crystalline, and the average size was ~10 nm. The obtained silicon nanoparticles had high purity, as the diamond abrasives included in the waste silicon powder were removed through oxidation and vaporization during laser irradiation.

1. Introduction

Silicon nanoparticles possess various unique and useful properties such as high photoluminescence (PL), intermediate band, large surface area, and biocompatibility, some of which are distinctly different from single-crystal bulk silicon [1,2]. These characteristics make silicon nanoparticles very useful in manufacturing of lithium-ion batteries, solar cells, biomedical devices, and other high value-added products [3–6]. For example, crack propagation in lithium-ion batteries during lithiation and delithiation processes can be prevented by the use of an anode made of silicon nanoparticles [7–11]. This crack propagation has been a severe problem in a conventional anode of bulk or thin film silicon [12].

One of the common methods to fabricate silicon nanoparticles is chemical vapor deposition (CVD) [13], but it is difficult to fabricate high-purity silicon nanoparticles since silicon nanoparticles react with precursor gases during the chemical reaction. In addition to CVD, femtosecond pulsed laser irradiation on a single-crystal silicon wafer was applied to generate silicon nanoparticles with high purity and

uniform sizes [14,15]. However, femtosecond laser ablation of a silicon wafer is expensive and very time-consuming.

In this study, we propose nanosecond pulsed laser irradiation of waste silicon powder to generate high-purity silicon nanoparticles at low cost. Currently, in the manufacturing process of single- or poly-crystal silicon wafers for semiconductor devices and solar cells, silicon ingots are sliced using a multi-wire saw. During the slicing process, a large quantity of silicon sludge powder, the average size of which is in the micrometer level, is produced and disposed of as an industrial waste [16]. It is difficult to reuse these sludge powders for silicon ingot production due to the impurities from diamond abrasive grains and chemical agents in the slurry fluids. The objective of this study is to perform nanosecond pulsed laser irradiation on the waste silicon powder to generate silicon nanoparticles and at the same time to remove the impurities included in the silicon waste. If successful, the proposed method is eco-friendly, less expensive and much faster than silicon nanoparticle generation by femtosecond pulsed laser irradiation of silicon wafers.

In this study, nanosecond pulsed laser irradiation through a glass substrate was attempted on the waste silicon powder target, and the

* Corresponding author. Department of Mechanical Engineering, Faculty of Science and Technology, Keio University, Hiyoshi 3-14-1, Kohoku-ku, Yokohama, 223-8522, Japan.

E-mail address: yan@mech.keio.ac.jp (J. Yan).

<https://doi.org/10.1016/j.mssp.2020.104998>

Received 31 October 2019; Received in revised form 7 February 2020; Accepted 10 February 2020
1369-8001/© 2020 Elsevier Ltd. All rights reserved.

generated nanoparticles were collected by the glass substrate based on backward transfer. The distance between the glass substrate and the target was varied and the change of particle size and morphology were investigated. The crystallinity and size of the generated silicon nanoparticles were characterized by Raman spectroscopy and transmission electron microscopy (TEM). In addition, the laser-induced changes of the diamond abrasive grains were investigated to examine the capability of impurity removal by laser irradiation. This study will demonstrate the possibility of fabricating uniform and high-purity silicon nanoparticles from industrial waste at low production cost.

2. Experimental procedure

The waste silicon powder used in this experiment was obtained from a multi-wire sawing process of single-crystal silicon ingots and had a mean size of 2.8 μm . For the preparation of laser irradiation target, waste silicon powder was coated on a silicon wafer (size: 30 mm \times 30 mm) so that the laser beam can be irradiated uniformly on the waste silicon powder. Before coating, the mixture of waste silicon powder and an organic solvent of N-methyl-2-pyrrolidone were agitated by a ball mill to obtain a slurry. The slurry was deposited on the silicon wafer with a thickness of 100 μm and dried at 100 $^{\circ}\text{C}$ for 2 h. In preliminary laser irradiation tests, the depth of the laser-induced grooves on the deposited layer was about 10 μm for a single laser scan at high fluence conditions. Hence, the deposited layer (100 μm) was thick enough to protect the silicon substrate from laser processing.

A nanosecond pulsed Nd:YAG laser excited by a laser diode, LR-SHG, produced by MEGAOPTO Co., Ltd, Japan, was used for experiments. The laser has a wavelength of 532 nm, a repetition frequency of 10 kHz, a pulse width of 48.4 ns and a focused beam spot diameter of 85 μm . The beam has a Gaussian energy distribution, as shown in Fig. 1. The laser beam was scanned using a galvanometer mirror system. The scan speed of the laser beam and laser fluence were set to 1 mm/s and 1.1 J/cm² respectively. As illustrated in Fig. 2, the generated silicon nanoparticles were collected on a 1.5 mm-thick soda-lime glass substrate placed above the irradiated target. Soda-lime glass has high transparency of above 90% to the laser wavelength of 532 nm. After laser irradiation, the glass substrate was examined by a microscope and no crack or groove was found on the glass surface. Thus, the glass substrate was not machined by laser and did not take part in the synthesis process of silicon nanoparticles.

The glass substrate was set on a base which has an inclined angle θ of 0.9 $^{\circ}$ to the target surface, so that the substrate-target distance d can be

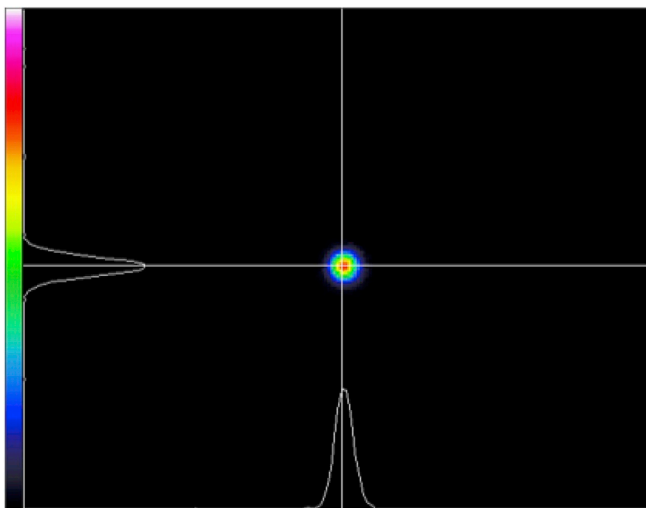


Fig. 1. Gaussian energy density distribution of laser beam used in the experiment.

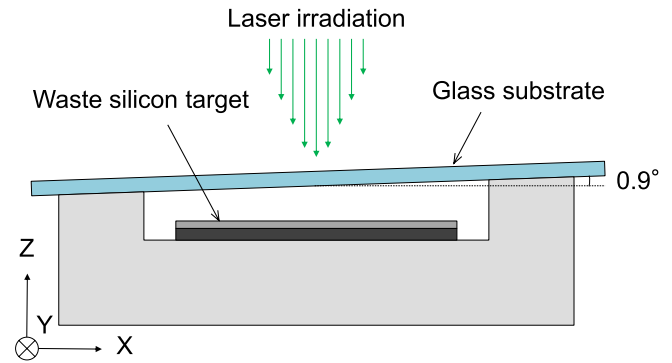


Fig. 2. Experimental setup of laser irradiation through a glass substrate placed on a base with an inclined angle.

adjusted from 10 to 500 μm by scanning the laser beam at different X coordinates. The substrate-target distance d was calculated by the following equation:

$$d = d_{\text{in}} + x \tan \theta - t \quad (1)$$

where d_{in} is the initial distance between the glass substrate and the silicon wafer, x is the arbitrary X coordinate, and t is the thickness of coating layer of waste silicon powder. The experimental parameters are summarized in Table 1.

After the laser irradiation, the surface topography of the deposited glass substrate was measured with a laser confocal microscope OLS4100 (Olympus Corp., Japan). From the measurement results, a cross-sectional profile was obtained and deposition amount per a unit time was calculated. Subsequently, the silicon nanoparticles deposited on the glass substrate were observed using scanning electron spectroscopy (SEM) Inspect F50 (FEI Company, USA) and MERLIN Compact (Carl Zeiss AG, Germany). Raman spectroscopy was performed to analyze the characteristics of silicon nanoparticles such as crystallinity and size distribution using a laser micro-Raman spectrometer NRS-3100 (JASCO Co., Japan). The wavelength of the laser used for the Raman spectrometer was 532 nm.

In order to obtain the size distribution of silicon nanoparticles from the Raman analysis result, silicon nanoparticle embedding was performed. As the silicon nanoparticles deposited on glass are not concentrated enough to perform Raman scattering, silicon nanoparticles were embedded into a carbon tape to concentrate the nanoparticles. The schematic diagram of embedding silicon nanoparticles is shown in Fig. 3. Silicon nanoparticles deposited on the glass substrate were concentrated using a spatula (Fig. 3a), and the concentrated silicon nanoparticles were embedded on a piece of carbon tape (Fig. 3b) for Raman mapping. Moreover, the size of silicon nanoparticles was confirmed using transmission electron microscopy (TEM) Tecnai G2 (FEI Company, USA).

Furthermore, the response of diamond grains contained in the silicon

Table 1
Laser irradiation conditions.

Parameter	Value
Wavelength (nm)	532
Environment	In air
Beam profile	Gaussian
Beam diameter (μm)	85
Repetition frequency (kHz)	10
Pulse width (ns)	48.4
Average power (mW)	600
Laser fluence (J/cm ²)	1.1
Number of pulse per unit area	850
Scan speed (mm/s)	1
Substrate-target distance(μm)	10, 100, 200, 300, 400, 500

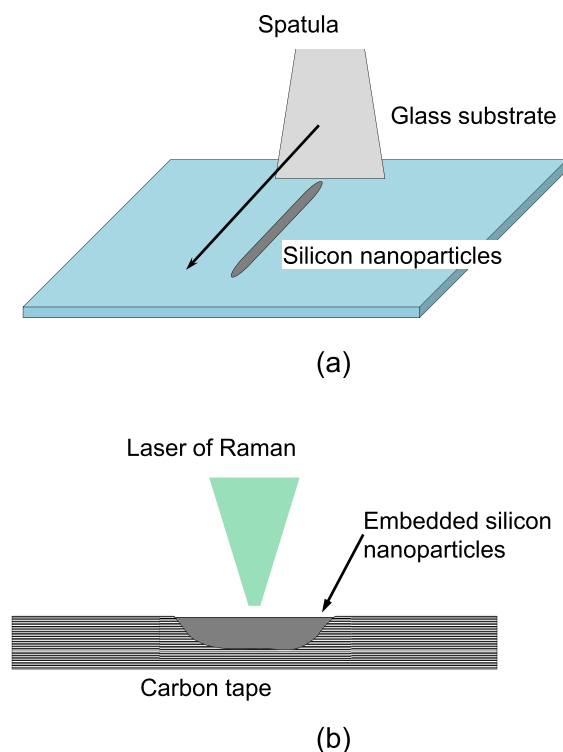


Fig. 3. Schematic diagram of sample preparation for Raman mapping: (a) concentrating silicon nanoparticles using a spatula, (b) embedding silicon nanoparticles inside a carbon tape.

waste during laser irradiation was investigated. As it was extremely difficult to find and locate a single diamond grain in the waste powder, a thin layer of diamond grains (grain size $\sim 10 \mu\text{m}$, the same as those used for wire saw fabrication) were deposited on a silicon substrate, and laser irradiation was performed. The experimental parameters are summarized in Table 2. The change of the diamond grains was evaluated by the laser microscope and the laser micro-Raman spectrometer.

3. Results and discussion

3.1. Effect of substrate-target distance

Fig. 4 shows surface topographies of the glass substrate after laser irradiation at various substrate-target distances. Large debris with a size of $10\text{--}60 \mu\text{m}$, which is larger than the original size of waste silicon powder, and a non-spherical shape were deposited at the substrate-target distance of $10 \mu\text{m}$ (Fig. 4a): In contrast, there were no such large debris at a distance of $500 \mu\text{m}$ (Fig. 4b).

The possible mechanisms of particle deposition at various substrate-target distances are schematically shown in Fig. 5. As melting and joining of waste silicon powders occur during laser irradiation, a melt

pool was generated due to the aggregation of melted waste silicon powder, which then received a recoil pressure from laser-induced plasma [17]. Consequently, melted silicon was scattered towards the glass substrate due to the recoil pressure (Fig. 5a). When the substrate-target distance was small, large debris scattered by laser would be deposited on the glass substrate (Fig. 5b); whereas when the substrate-target distance was large enough, large debris were redeposited on the target surface due to gravity (Fig. 5c). From this result, it can be concluded that to deposit only nanoparticles on the glass substrate, it is essential to use a sufficiently large substrate-target distance.

Next, by measuring surface topography, cross-sectional profiles of the deposits of silicon particles were obtained. Fig. 6a is a laser microscope surface topography showing particles deposited on a glass substrate at a substrate-target distance of $100 \mu\text{m}$. It can be seen that a band of silicon nanoparticles has been deposited on the glass and covered with a few big debris. Then, a cross-sectional profile was taken along the line AB to calculate the thickness of the deposition. The cross-sectional profiles of depositions obtained at various substrate-target distances are shown in Fig. 6b. As the substrate-target distance increased up to $200 \mu\text{m}$, the height of deposits in the Z direction decreased drastically. When the substrate-target distance further increased, the deposit height decrease was insignificant. It is also noticeable that silicon particles were scattered to a greater extent than the laser spot size in the horizontal direction when the substrate-target distance was large. Moreover, the deposition amount per unit time was calculated by the following equation:

$$V_{\text{deposit}} = v \times A_{\text{deposit}} \quad (2)$$

where V_{deposit} is deposition volume per unit time, v the scan speed of laser beam and A_{deposit} the cross-sectional area of deposits which was calculated from the cross-sectional profiles shown in Fig. 6b. As shown in Fig. 6c, V_{deposit} decreases sharply as the distance increases to $200 \mu\text{m}$, and then decreases gradually with further increase of the distance.

Furthermore, morphology of deposited silicon particles was examined, as illustrated in Fig. 7. Throughout the whole range of the substrate-target distances, deposited silicon particles adhered to each other. However, changing the substrate-target distance resulted in a change in deposition morphology. Laser irradiation at a target-substrate distance of less than $400 \mu\text{m}$ led to agglomerated structures as presented in Fig. 7a–d. In contrast, laser irradiation at a distance of $400 \mu\text{m}$ or more led to web-like structures as presented in Fig. 7e–f. As the substrate distance was increased, the deposited web-like structures became looser. Fig. 8 is a high-magnification image of Fig. 7f. It is seen that the deposited silicon particles have an average size of $\sim 25 \text{nm}$: including coating layer of Osmium to make the samples conductive. This means that the irradiation of nanosecond pulsed laser has enabled 89% size reduction from the original waste silicon powder.

The particle size reduction might have been caused by a vaporization and rapid cooling process. The possible mechanism of nanoparticle deposition is illustrated in Fig. 9. After a laser pulse is irradiated on the waste silicon powder, a surface region of waste silicon powder is melted and the melted region grows deeper and deeper (Fig. 9b). Subsequently, the melted silicon turns to vapor and plasma due to the high energy density of laser (Fig. 9c). In the vapor and plasma, silicon nanoparticles are generated due to the formation and growth of nuclei during cooling (Fig. 9d). The vapor and plasma expands radially, and the scattered silicon nanoparticles are backward transferred and deposited on the glass substrate (Fig. 9e). During the vapor cooling (Fig. 9d), the molten nanoparticles might aggregate with each other. However, nanoparticle synthesis is a build-up method where clustered silicon atoms or molecules are cooled rapidly in several hundreds of nanoseconds [18]. Thus, the rapid cooling can restrain both of the growth of nuclei and the aggregation of molten silicon nanoparticles.

The agglomerated web-like structure was induced by the high surface energy of silicon nanoparticles. Generally, surface energy increases

Table 2
Laser irradiation conditions for diamond abrasive grains.

Parameter	Value
Wavelength (nm)	532
Environment	In air
Beam profile	Gaussian
Beam diameter (μm)	85
Repetition frequency (kHz)	150
Pulse width (ns)	38
Average power (W)	9.4
Laser fluence (J/cm^2)	1.1
Number of pulse per unit area	850
Scan speed (mm/s)	15

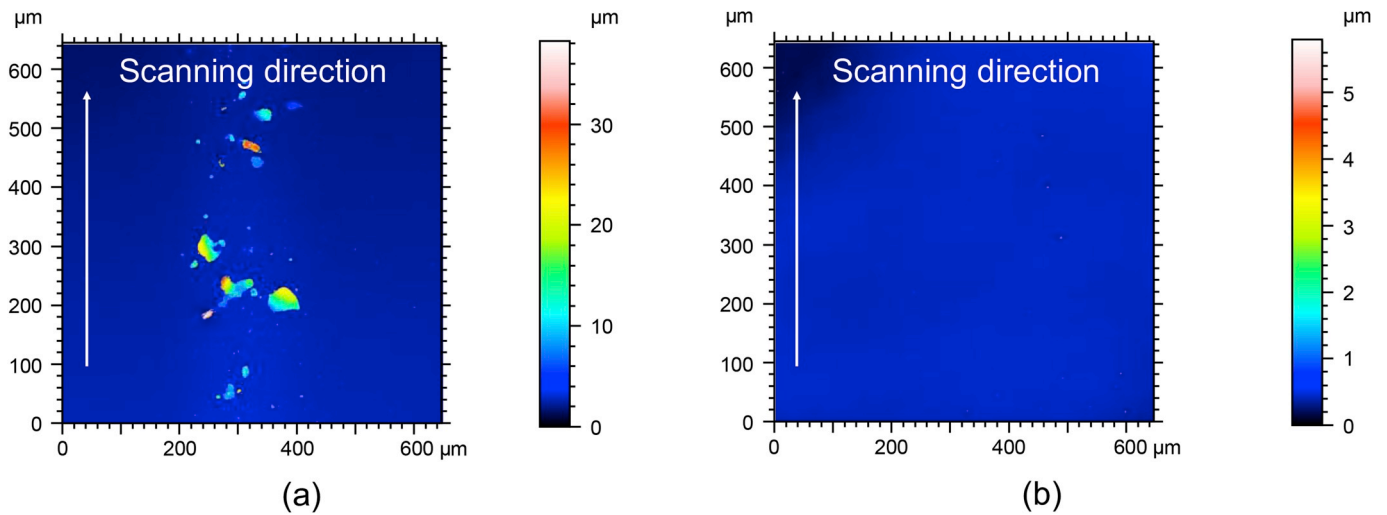


Fig. 4. Laser microscope surface topographies of deposits on glass substrates at different substrate-target distances: (a) 10 μm , (b) 500 μm .

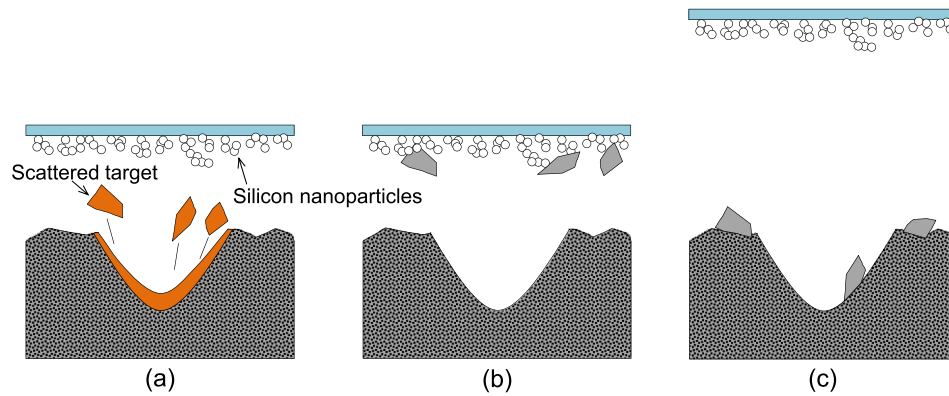


Fig. 5. Schematic of debris reduction by increasing the substrate-target distance: (a) scatter of melted waste silicon powder as debris, (b) debris deposition at a shorter substrate-target distance, (c) restraint of debris deposition at a longer substrate-target distance.

with decreasing particle size because a relatively large fraction of component atoms is located at the surface compared to a bulk material [19]. Therefore, a nanoparticle has high surface energy, which results in an adhesive property, leading to silicon nanoparticles agglomeration [15,20,21]. On the other hand, when silicon nanoparticles scatter into the air, friction between silicon nanoparticles and air molecules occurs. This friction leads to electrostatic force, which is dominant compared to the gravity in the case of the nanometer level [22]. When the particle traveling distance increases, the electrostatic force increases as silicon nanoparticles are scattered over a longer distance and collide with more molecules of air. As a result, the electrostatic force becomes locally higher than the adhesive force, which leads to the generation of loose web-like structures of silicon nanoparticles.

3.2. Cross-sectional observation of deposited area

Fig. 10 shows a back scattered electron image of deposited silicon nanoparticles observed from cross-sectional direction to the deposited area at the substrate-target distance of 100 μm . The thickness of the deposited layer was 250–500 nm, as presented in Fig. 10a. In addition, as illustrated in Fig. 10b, relatively large nanoparticles, with a size of over 30 nm, were stuck in top layer composed of branches of silicon nanoparticles. This might have been caused by drag force. When a spherical particle with the radius of r moves in a stationary gaseous medium with mean free path of λ , in the case of a small r in comparison with λ , slowing of the particle can be caused by the collective effects of

collisions with individual gas molecules, in which case Epstein's law is applied to drag force [23,24]. On the other hand, in the opposite case, a frictional force exerted by a viscous fluid affects particle slowing, whereby Stokes drag force is applied. In this experiment, the size of silicon nanoparticles is smaller than mean free path of air, $\lambda = \sim 65$ nm, at atmospheric pressure. Hence, scattered silicon nanoparticles receive drag force as defined by Epstein, given by the following equation [23]:

$$f_d = -\frac{4}{3}\pi\sigma n \frac{m_g}{m_p} \hat{c} r^2 v_p \quad (3)$$

where f_d is a drag force of a scattered silicon nanoparticle, δ shows the interaction between the particle and a gas molecule, n is the number density of the gas, m_g and m_p are the mass of the gas molecule in air and the particle respectively, \hat{c} is the mean thermal velocity, r is the particle radius, and v_p is the velocity of the particle. As described in Equation (3), the drag force f_d is proportional to square of the particle radius r . This proportional relationship indicates that larger particles can be deposited on the top layer of the silicon nanoparticle branches which are deposited on the glass substrate beforehand.

3.3. Characterization of silicon nanoparticles

Fig. 11 a shows the typical peaks of silicon nanoparticles and a single-crystal silicon wafer as a reference, obtained by Raman scattering spectroscopy. The spectra indicate that silicon nanoparticles have a peak at 520.2 cm^{-1} , which is close to the single crystalline silicon peak at 521

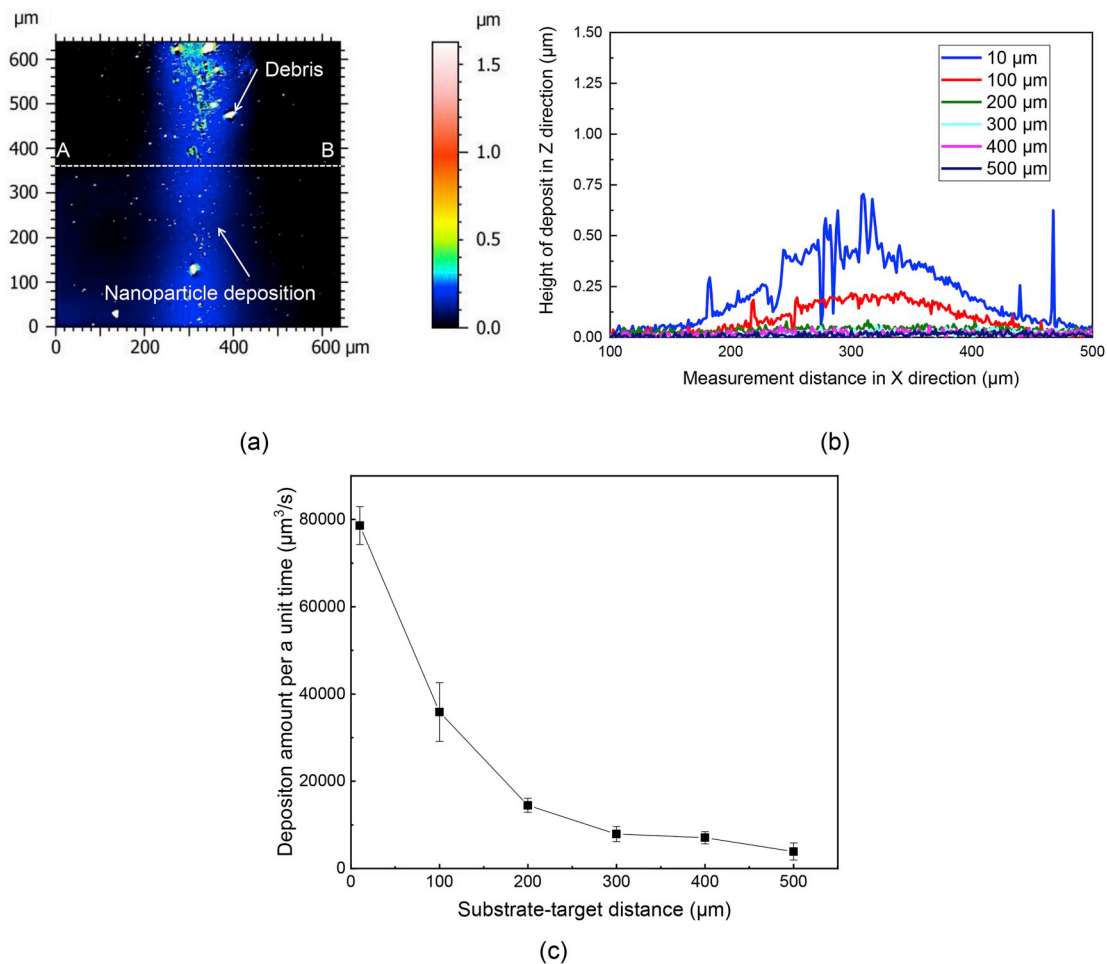


Fig. 6. (a) Laser microscope surface topography of silicon deposits on a glass substrate at a substrate-target distance of 100 μm; (b) cross-sectional profile of the deposited layer at various substrate-target distance; (c) deposition volume per unit time at different substrate-target distances.

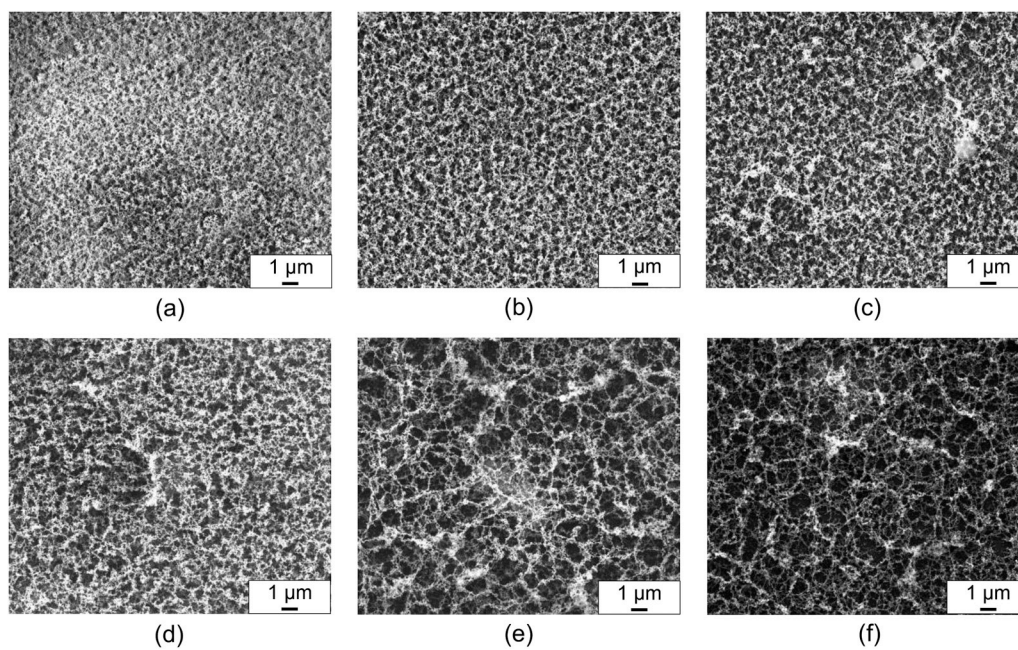


Fig. 7. Deposition morphology of silicon nanoparticles at the different substrate-target distances: (a) 10 μm, (b) 100 μm, (c) 200 μm, (d) 300 μm, (e) 400 μm, (f) 500 μm.

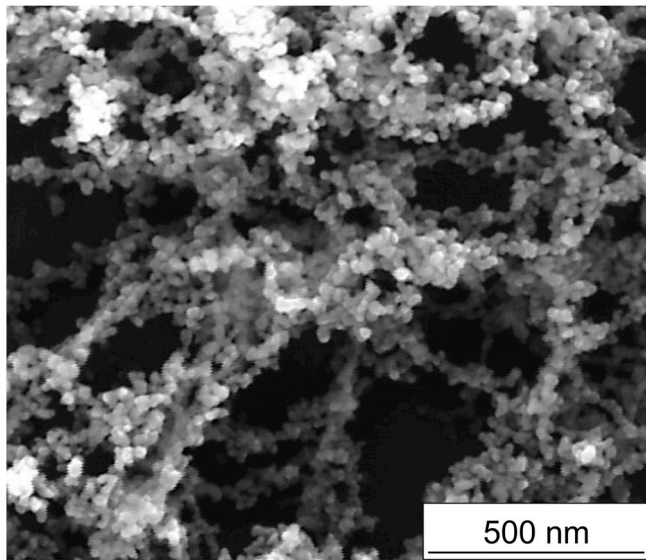


Fig. 8. High-magnification image of silicon nanoparticles at a substrate-target distance of 500 μm .

cm^{-1} [25]. The peak shift can be explained by the phonon confinement model [26–29]. According to this model, the peak of silicon nanoparticles in the Raman spectra shifts into low-wavenumber side compared with that of single-crystal bulk silicon. In addition, full width at half maximum (FWHM) of silicon nanoparticles increases. This is caused by the localization of the phonon which leads to the breakdown of the $q = 0$ selection rule. The peak shift is related to the size of the silicon nanoparticle. The peak shift of silicon nanoparticles can be

calculated by using the following equation [27]:

$$\Delta\omega = -52.3 \left(\frac{0.543}{D} \right)^{1.586} \quad (4)$$

where $\Delta\omega$ is the peak shift of a silicon nanoparticle and D is the diameter (size) of the silicon nanoparticle. Based on this equation, the peak shift of 0.8 cm^{-1} indicated that the size of generated silicon nanoparticles was 7.8 nm.

Moreover, Raman mapping was carried out in order to analyze the silicon nanoparticles in a greater area. Fig. 12a shows the surface micrograph of silicon nanoparticles embedded in a carbon tape. The region surrounded by the red box was characterized by Raman mapping. Fig. 12b illustrates the Raman mapping result of peak shift. In the whole analyzed area, the peak of silicon nanoparticles ranged between 520.2 and 520.8 cm^{-1} . This result indicates that the silicon nanoparticles are uniform and independent, rather than being bonded together forming clusters. This might be due to the formation of an extremely thin oxide layer on the surface of each nanoparticle which prevented inter-particle bonding. Finally, the size distribution histogram was obtained using Equation (4), as presented in Fig. 12c. In addition, the minimal and maximal size, mean size, maximum of distribution, FWHM and dispersion were summarized in Table 3. It was established that the particle size distribution can be described by the Voigt function [14]: a convolution of Gaussian and Lorentzian function [30]. As shown in Fig. 12c, a narrow distribution was achieved, where the maximum of distribution was 13.9 nm, and minimal size of silicon nanoparticles reached the single-nanometer level (7.8 nm). This narrow size distribution is due to the short time scale of laser interaction. During the nuclei growth in silicon vapor, the generated silicon nanoparticles are cooled and deposited rapidly, so that they do not interfere with the subsequently generated nanoparticles. In other words, nuclei formation does not

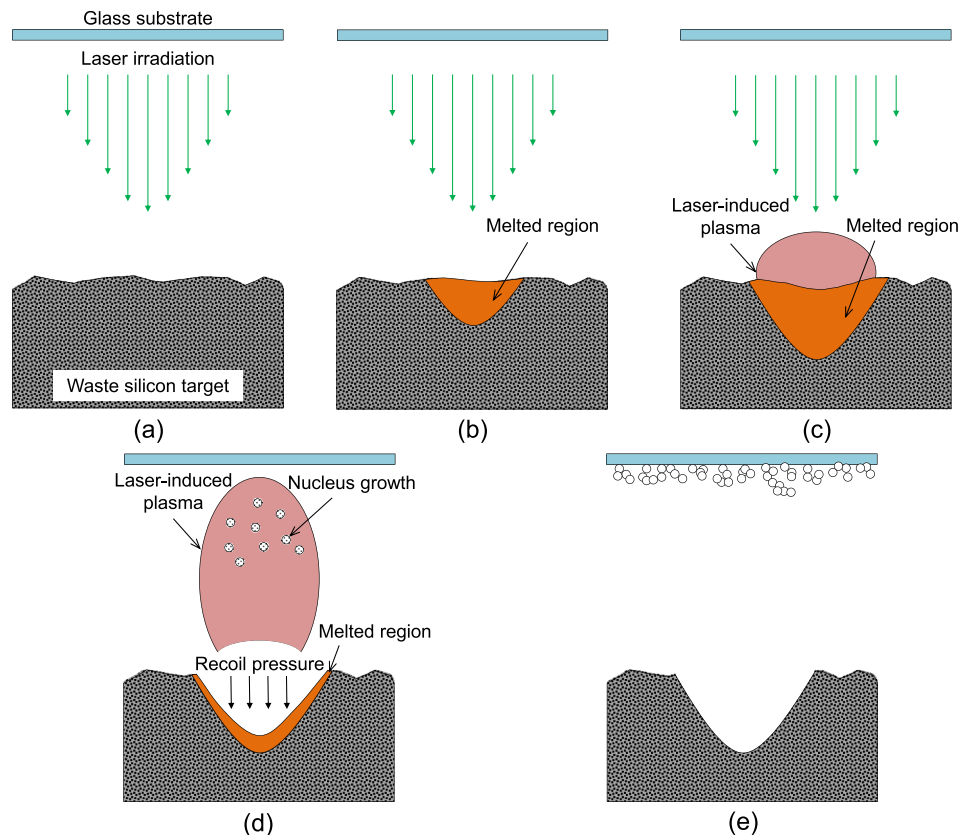
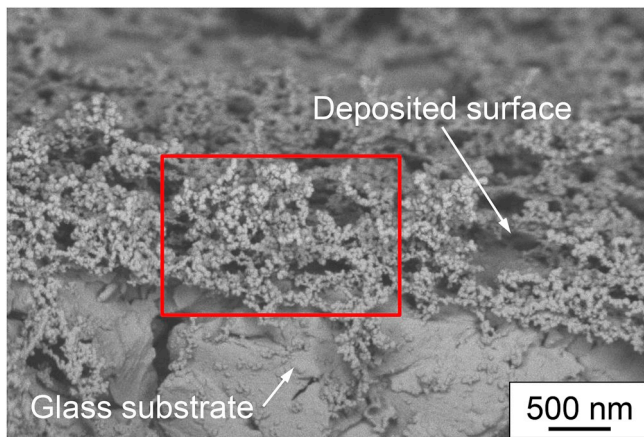
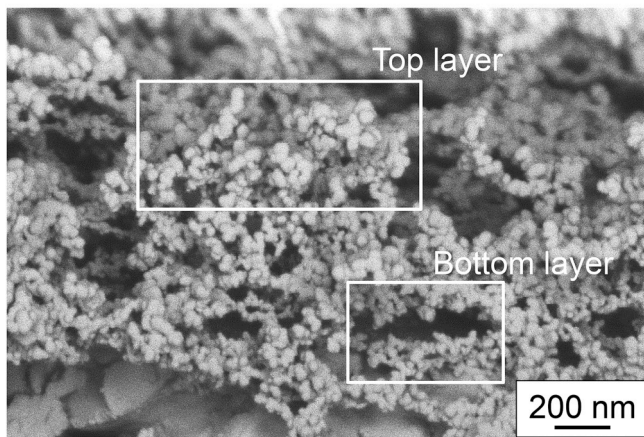


Fig. 9. Mechanism of generation and deposition of silicon nanoparticles: (a) laser irradiation through a glass substrate, (b) formation of melted region, (c) generation of laser-induced plasma, (d) plasma expansion and nucleus growth, (e) deposition of silicon nanoparticles.



(a)



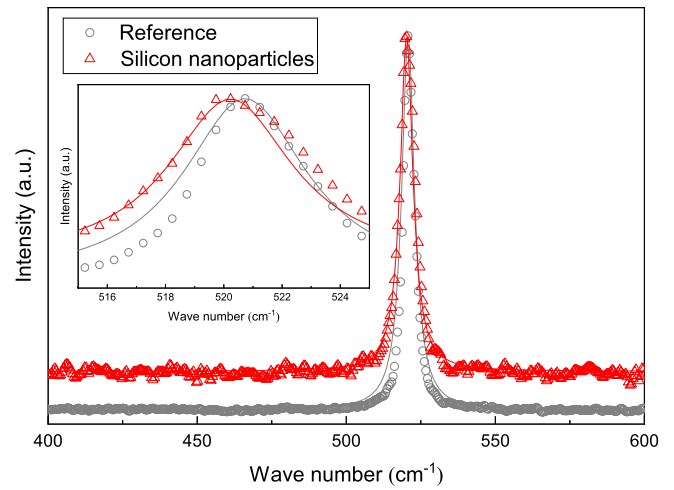
(b)

Fig. 10. (a) Cross-sectional observation of deposited silicon nanoparticles, (b) high-magnification image of the region surrounded in red line in (a).

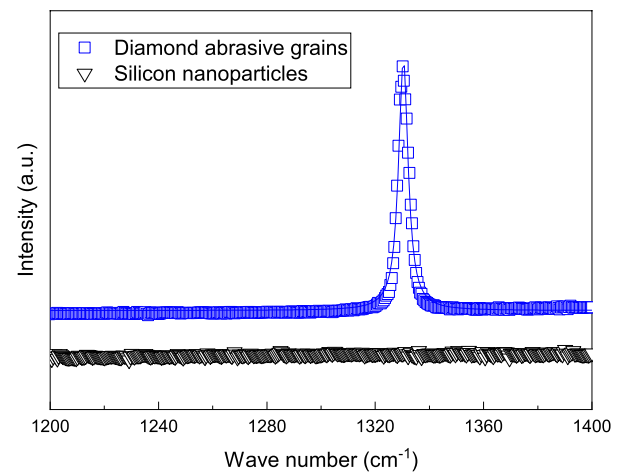
occur during the growing process of silicon nanoparticles. If new nuclei are formed during the growing process, the growing speed of new nuclei is delayed compared with that of the initial nuclei, resulting in wide size distribution.

It should be pointed out that no impurity like carbon was detected from the Raman analysis, as presented in Fig. 11b, indicating oxidation and vaporization of diamond abrasives included in the waste silicon powder during laser irradiation. When silicon turns to plasma phase, its temperature exceeds 6000 K, which is above the sublimation temperature of diamond 3900 K [31]. Hence, the high temperature causes diamond to evaporate. It is also presumable that the generated silicon nanoparticles have core-shell structure where nanocrystalline silicon is covered with a very thin oxide layer. The oxidation of silicon nanoparticles is likely to be caused by overheating during the laser irradiation process. Additionally, oxidation occurs due to higher ratio of surface atoms to total atoms in silicon nanoparticles [3,32]. Surface atoms act as defects known as dangling bonds due to the absence of bonding partner. Since oxidation of the surface of silicon nanoparticles stabilizes dangling bonds, the oxidation of silicon nanoparticles occurs easily in the atmosphere.

Furthermore, TEM observation was performed to confirm that the size of silicon nanoparticles measured by Raman spectroscopy corresponds to the actual size of them. Fig. 13 shows that silicon nanoparticles are agglomerated each other. According to this result, the size distribution of silicon nanoparticles was calculated, where arbitrary silicon nanoparticles in Fig. 13 were extracted randomly. Fig. 14



(a)



(b)

Fig. 11. Raman spectra of silicon nanoparticles: (a) lower wave number side, (b) higher wave number side.

describes calculated size distribution of silicon nanoparticles by TEM observation. The minimal and maximal size, mean size, maximum of distribution, FWHM and dispersion were summarized in Table 4. The result calculated by TEM observation was consistent with that calculated by Raman spectroscopy, whereas mean of the distribution was slightly shifted to a smaller value as compared with Table 3.

3.4. Response of diamond abrasive grains

Next, laser irradiation was performed on diamond grains to investigate the laser-induced changes of the diamond abrasives included in the silicon waste. Fig. 15 shows a three-dimensional surface topography of diamond abrasive grains deposited on a silicon substrate after laser irradiation in the center region. It is clear that after laser irradiation, most of diamond abrasive grains disappeared. In addition, Raman scattering spectroscopy was carried out, as presented in Fig. 16. In the laser-affected region, no significant peak of single-crystal diamond was detected.

These results demonstrated that diamond abrasive grains included in the silicon waste could be removed as carbon dioxide gas. This might be a result of the phase transformation, vaporization and chemical reaction with oxygen during laser irradiation. In the laser-induced plasma, diamond grains undergo diamond-graphite transformation and

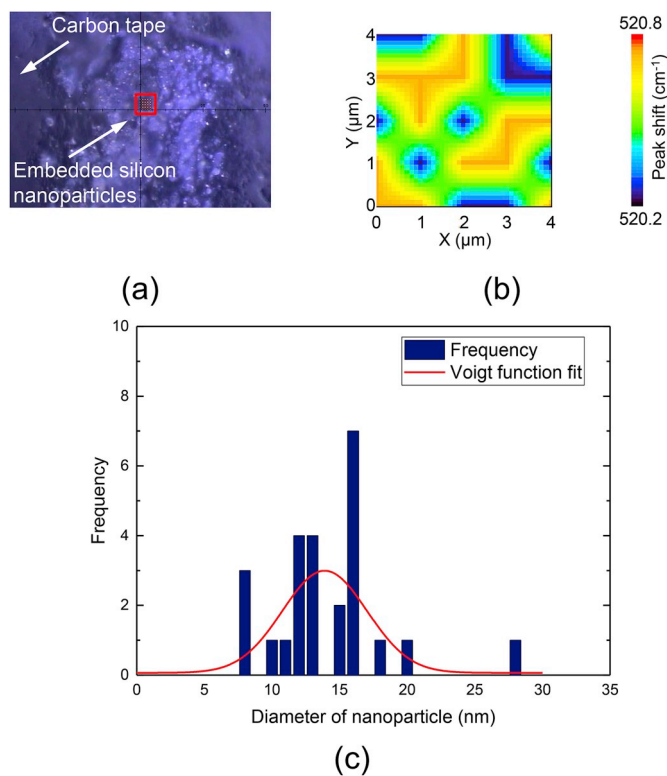


Fig. 12. (a) Surface micrograph, (b) mapping of peak shift at 521 cm⁻¹, (c) size distribution histogram of silicon nanoparticles.

Table 3
Analysis results of silicon nanoparticles.

Minimal size (nm)	7.8
Maximal size (nm)	27.2
Mean size (nm)	13.7
Maximum of distribution (nm)	13.9
FWHM (nm)	7.4
Dispersion	16.9

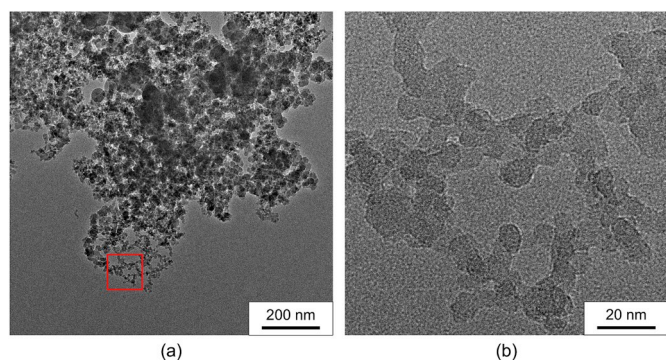


Fig. 13. (a) TEM image of generated silicon nanoparticles, (b) high-magnification image of the region surrounded in the red line in (a).

vaporization. The vaporized carbon element reacts with oxygen in air, generating carbon dioxide gas. Carbon reacts with oxygen more easily than with silicon since the enthalpy of carbon-dioxide formation is much lower than that of silicon-carbide formation [33,34]. This situation is different from the reaction sintering process where SiC formation occurs by nanosecond pulsed laser irradiation on pellets of a stoichiometric powder mixture of Si and C under Ar gas flow [35]. The laser-induced removal of diamond abrasive grains from waste silicon powders helps

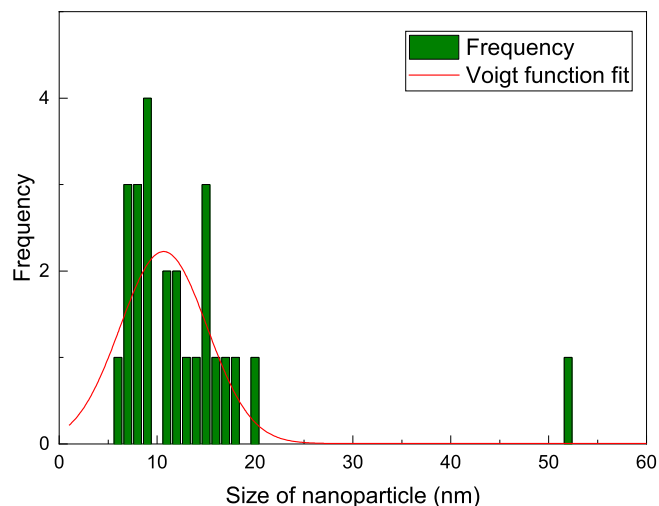


Fig. 14. Size distribution histogram of silicon nanoparticles measured by TEM observation.

Table 4
Summary of size distribution calculated by TEM observation.

Minimal size (nm)	5.5
Maximal size (nm)	51.9
Mean size (nm)	12.7
Maximum of distribution (nm)	10.7
FWHM (nm)	10.5
Dispersion	8.9

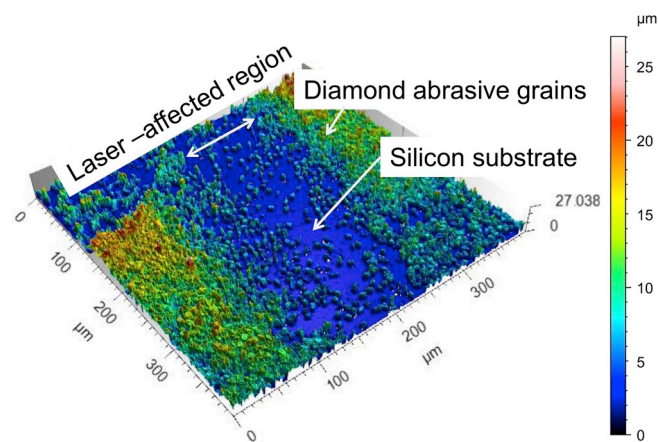


Fig. 15. Three-dimensional surface topography of diamond abrasive grains on silicon substrate after laser irradiation.

improve the purity of generated silicon nanoparticles.

4. Conclusions

Nanosecond pulsed Nd:YAG laser irradiation was performed on waste silicon powder to generate silicon nanoparticles. The morphology and crystallinity of the generated silicon nanoparticles were characterized using Raman spectroscopy. The following conclusions were obtained.

- (1) Silicon nanoparticles were deposited on the glass substrate in the whole experimental range of the substrate-target distances. There was no micrometer-scale particle deposition at a substrate-target distance of 500 μm or bigger.

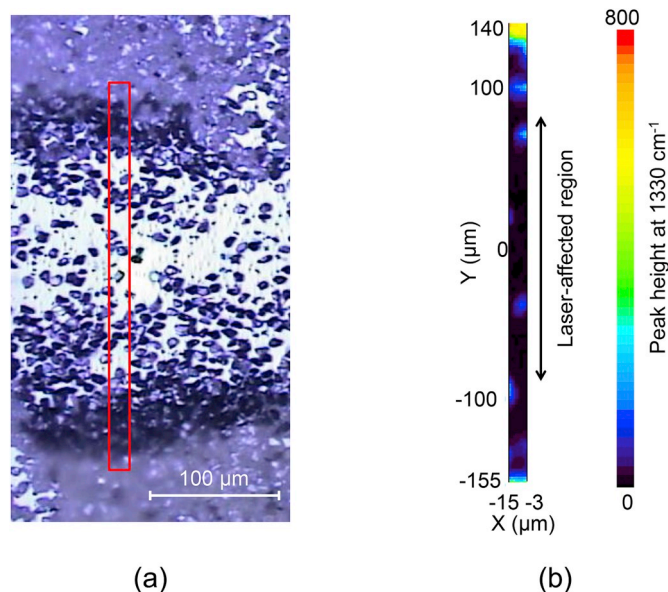


Fig. 16. (a) Surface micrograph, (b) mappings of peak height at 1330 cm^{-1} of diamond abrasive grains after laser irradiation.

- (2) As the substrate-target distance was increased, the deposition amount per unit time decreased and the deposition nanoparticle morphology was shifted from an agglomerated structure to a web-like structure.
- (3) Larger nanoparticles were stuck in the top layer as nanoparticle branches while smaller nanoparticles are deposited independently in the bottom layer.
- (4) The obtained silicon nanoparticles had a crystalline structure covered by a thin layer of silicon oxide. The maximum of size distribution was 13.9 nm and the minimal size was 7.8 nm.
- (5) No impurity was detected from the nanoparticles. The diamond abrasives included in the waste silicon powders could be removed through vaporization and oxidation during laser irradiation.

Declaration of competing interest

The authors declare that they have no known competing financial interests or personal relationships that could have appeared to influence the work reported in this paper.

CRediT authorship contribution statement

Ko Momoki: Investigation, Data curation, Writing - original draft. **Takeshi Manabe:** Resources. **Lin Li:** Writing - review & editing. **Jiawang Yan:** Conceptualization, Methodology, Supervision, Writing - review & editing.

Acknowledgments

This study has been financially supported by Japan Society for the Promotion of Science, Grant-in-Aid for Exploratory Research, 17K18833 (2017–2019). Yan and Li are grateful for the Leverhulme Trust (UK), Grant Reference Number VP1-2018-022.

References

- [1] D.E. Harwell, J.C. Croney, W. Qin, J.T. Thornton, J.H. Day, E.K. Hajime, D. M. Jameson, Effects of surface passivation on silicon nanoparticle photoluminescence, *Chem. Lett.* 32 (2003) 1194, <https://doi.org/10.1246/cl.2003.1194>.
- [2] Q. Wang, Y. Bao, X. Zhang, P.R. Coxon, U.A. Jayasooriya, Y. Chao, Uptake and toxicity studies of poly-acrylic acid functionalized silicon nanoparticles in cultured mammalian cells, *Adv. Healthc. Mater.* 1 (2012) 189, <https://doi.org/10.1002/adhm.201100010>.
- [3] J.A. Carlisle, I.N. Germanenko, Y.B. Pithawalla, M.S. El-Shall, Morphology, photoluminescence and electronic structure in oxidized silicon nanoclusters, *J. Electron. Spectrosc. Relat. Phenom.* 114–116 (2001) 229, [https://doi.org/10.1016/S0368-2048\(00\)00399-6](https://doi.org/10.1016/S0368-2048(00)00399-6).
- [4] H.R. Rasouli, A. Ghobadi, T.G. Ulusoy Ghobadi, H. Ates, K. Topalli, A.K. Okayay, Nanosecond pulsed laser ablated sub-10 nm silicon nanoparticles for improving photovoltaic conversion efficiency of commercial solar cells, *J. Optic.* 19 (2017) 6, <https://doi.org/10.1088/2040-8986/aa84dd>.
- [5] X.Y. Chen, Y. Lu, Y.H. Wu, B.J. Cho, M.H. Liu, D.Y. Dai, W.D. Song, Mechanisms of photoluminescence from silicon nanocrystals formed by pulsed-laser deposition in argon and oxygen ambient, *J. Anal. At. Spectrom.* 93 (2003) 6311, <https://doi.org/10.1063/1.1569033>.
- [6] Y. Xin, T. Kitasako, M. Maeda, K.-I. Saitow, Solvent dependence of laser-synthesized blue-emitting Si nanoparticles: size, quantum yield, and aging performance, *Chem. Phys. Lett.* 974 (2017) 90, <https://doi.org/10.1016/j.cplett.2017.02.060>.
- [7] L. Hu, H. Wu, S. Sae Hong, L. Cui, J.R. McDonough, S. Bohy, Y. Cui, Si nanoparticle-decorated Si nanowire networks for Li-ion battery anodes, *Chem. Commun.* 47 (2011) 367, <https://doi.org/10.1039/c0cc02078h>.
- [8] J. Sourice, A. Bordes, A. Boulineau, J.P. Alper, S. Franger, A. Quinsac, A. Habert, Y. Leconte, E. De Vito, W. Porcher, C. Reynaud, N. Herlin-Boime, C. Haon, Core-shell amorphous silicon-carbon nanoparticles for high performance anodes in lithium ion batteries, *J. Power Sources* 328 (2016) 527, <https://doi.org/10.1016/j.jpowsour.2016.08.057>.
- [9] S. Goriparti, E. Miele, F. De Angelis, E. Di Fabrizio, R. Proietti Zaccaria, C. Capiglia, Review on recent progress of nanostructured anode materials for Li-ion batteries, *J. Power Sources* 257 (2014) 421, <https://doi.org/10.1016/j.jpowsour.2013.11.103>.
- [10] J. Lee, J. Koo, B. Jang, S. Kim, Quantitative relationships between microstructures and electrochemical properties in Si core-SiO₂ shell nanoparticles for Li-ion battery anodes, *J. Power Sources* 329 (2016) 79, <https://doi.org/10.1016/j.jpowsour.2016.08.035>.
- [11] B.J. Dimitrijevic, K.E. Aifantis, K. Hackl, The influence of particle size and spacing on the fragmentation of nanocomposite anodes for Li batteries, *J. Power Sources* 206 (2012) 343, <https://doi.org/10.1016/j.jpowsour.2012.01.065>.
- [12] M.J. Chon, V.A. Sethuraman, A. McCormick, V. Srinivasan, P.R. Guduru, Real-time measurement of stress and damage evolution during initial lithiation of crystalline silicon, *Phys. Rev. Lett.* 107 (2011), <https://doi.org/10.1103/PhysRevLett.107.045503>.
- [13] A. Soni, L. Zhao, H.Q. Ta, Q. Shi, J. Pang, P.S. Wrobel, T. Gemming, A. Bachmatiuk, M.H. Rummeli, Facile graphitization of silicon nano-particles with ethanol based chemical vapor deposition, *Nano-Structures & Nano-Objects* 16 (2018) 38, <https://doi.org/10.1016/j.NANOSO.2018.04.001>.
- [14] F.V. Kashayev, T.P. Kaminskaya, L.A. Golovan, Structural properties of silicon nanoparticles obtained via femtosecond laser ablation in gases at different pressures, *Opt. Quant. Electron.* 48 (2016), <https://doi.org/10.1007/s11082-016-0617-8>.
- [15] E.I. Ageev, D.V. Potorochin, D.V. Sachenko, G.V. Odintsova, Generation of web-like structures and nanoparticles by femtosecond laser ablation of silicon target in ambient air, *Opt. Quant. Electron.* 49 (2017) 40, <https://doi.org/10.1007/s11082-016-0875-5>.
- [16] A. Yoko, Y. Oshima, Recovery of silicon from silicon sludge using supercritical water, *J. Supercrit. Fluids* 75 (2013) 1, <https://doi.org/10.1016/J.SUPFLU.2012.12.019>.
- [17] J.Y. Xu, H. Hu, Y.L. Lei, Morphological features of silicon substrate by using different frequency laser ablation in air and water, *Appl. Surf. Sci.* 317 (2014) 666, <https://doi.org/10.1016/j.apsusc.2014.08.038>.
- [18] O.A. Ranjbar, Z. Lin, A.N. Volkov, "One-dimensional kinetic simulations of plume expansion induced by multi-pulse laser irradiation in the burst mode at 266 nm wavelength, *Vacuum* 157 (2018) 361, <https://doi.org/10.1016/J.VACUUM.2018.08.065>.
- [19] H. Krupp, Particle adhesion theory and experiment, *Adv. Colloid Interface Sci.* 1 (1967) 111, [https://doi.org/10.1016/0001-8686\(67\)80004-6](https://doi.org/10.1016/0001-8686(67)80004-6).
- [20] G. Odachi, R. Sakamoto, K. Hara, T. Yagi, Effect of air on debris formation in femtosecond laser ablation of crystalline Si, *Appl. Surf. Sci.* 282 (2013) 525, <https://doi.org/10.1016/J.APSUSC.2013.06.005>.
- [21] T. Matsumura, A. Kazama, T. Yagi, Generation of debris in the femtosecond laser machining of a silicon substrate, *Appl. Phys. A* 81 (2005) 1393, <https://doi.org/10.1007/s00339-004-3192-y>.
- [22] M.S. El-Shall, Victor Abdelsayed, Y.B. Pithawalla, E. Alsharrah, S.C. Deevi, Vapor phase growth and assembly of metallic, intermetallic, carbon, and silicon nanoparticle filaments, *J. Phys. Chem. B* 107 (2003) 2882, <https://doi.org/10.1021/jp022176o>.
- [23] C.M. Rouleau, A.A. Puzetzy, D.B. Geohegan, Slowing of femtosecond laser-generated nanoparticles in a background gas, *Appl. Phys. Lett.* 105 (2014) 213108, <https://doi.org/10.1063/1.4902878>.
- [24] P.S. Epstein, On the resistance experienced by spheres in their motion through gases, *Phys. Rev.* 23 (1924) 710, <https://doi.org/10.1103/PhysRev.23.710>.
- [25] Y. Gogotsi, C. Baek, F. Kirscht, Raman microspectroscopy study of processing-induced phase transformations and residual stress in silicon, *Semicond. Sci. Technol.* 14 (1999) 936, <https://doi.org/10.1088/0268-1242/14/11/501>.
- [26] H. Richter, Z.P. Wang, L. Ley, The one phonon Raman spectrum IN microcrystalline silicon, *Solid State Commun.* 39 (1981) 625, [https://doi.org/10.1016/0038-1098\(81\)90337-9](https://doi.org/10.1016/0038-1098(81)90337-9).

- [27] V. Paillard, P. Puech, M.A. Laguna, R. Carles, B. Kohn, F. Huisken, Improved one-phonon confinement model for an accurate size determination of silicon nanocrystals, *J. Appl. Phys.* 86 (1999) 1921, <https://doi.org/10.1063/1.120648>.
- [28] J. Zi, K. Zhang, X. Xie, Comparison of models for Raman spectra of Si nanocrystals, *Phys. Rev. B* 55 (1997) 9263, <https://doi.org/10.1103/physrevb.55.9263>.
- [29] M.N. Islam, A. Pradhan, S. Kumar, Effects of crystallite size distribution on the Raman-scattering profiles of silicon nanostructures, *J. Appl. Phys.* 98 (2005), <https://doi.org/10.1063/1.120640>.
- [30] E.E. Whiting, An empirical approximation to the Voigt profile, *J. Quant. Spectrosc. Radiat. Transf.* 8 (1968) 1379, [https://doi.org/10.1016/0022-4073\(68\)90081-2](https://doi.org/10.1016/0022-4073(68)90081-2).
- [31] M. Milán, J.J. Laserna, Diagnostics of silicon plasmas produced by visible nanosecond laser ablation, *Spectrosc. Radiat. Transf.* 56 (2001) 275, [https://doi.org/10.1016/S0584-8547\(01\)00158-6](https://doi.org/10.1016/S0584-8547(01)00158-6).
- [32] Y. Kanemitsu, Light-emitting silicon materials, *J. Lumin.* 70 (1996) 333, [https://doi.org/10.1016/0022-2313\(96\)00068-3](https://doi.org/10.1016/0022-2313(96)00068-3).
- [33] N.J. Mammano, Heats of combustion and electron spin resonance of ultrafine graphite, *J. Solid State Chem.* 89 (1986), [https://doi.org/10.1016/0022-4596\(86\)90092-7](https://doi.org/10.1016/0022-4596(86)90092-7).
- [34] E. Greenberg, C.A. Natke, W.N. Hubbard, The enthalpy of formation of silicon carbide by fluorine bomb calorimetry, *J. Chem. Thermodyn.* 2 (1970) 193, [https://doi.org/10.1016/0021-9614\(70\)90083-2](https://doi.org/10.1016/0021-9614(70)90083-2).
- [35] S. Suehiro, T. Kimura, Rapid reaction sintering of silicon carbide using Nd:YAG laser, *J. Ceram. Soc. Jpn.* 127 (7) (2019) 504–506, <https://doi.org/10.2109/jcersj2.18191>.